How to Cite: Badaoui, M., Sehil, H., & Lamouri, C. (2025). Synthesis, Characterization, and Photocatalytic Activity of $CeBiO_3$ and $FeBiO_3$ Nanoparticles Prepared via the Sol-Gel Process. *Eurasian Journal of Chemistry, 30, 2(118), 85-94.* https://doi.org/10.31489/2959-0663/2-25-7

Article

Received: 31 March 2025 | Revised: 20 May 2025 | Accepted: 28 May 2025 | Published online: 4 June 2025

UDC 546.06+544.4

https://doi.org/10.31489/2959-0663/2-25-7

Mohamed Badaoui[1*], Hafida Sehil[2], Chaimaa Lamouri[2]

[1]*Synthesis and Catalysis Laboratory, University of Tiaret, Tiaret, Algeria;*
[2]*Department of Chemistry, Faculty of Sciences of the Matter, University of Tiaret, Tiaret, Algeria*
*(*Corresponding author's e-mail: mohamed.badaoui@univ-tiaret.dz)*

Synthesis, Characterization, and Photocatalytic Activity of $CeBiO_3$ and $FeBiO_3$ Nanoparticles Prepared via the Sol-Gel Process

This study investigated the photocatalytic potential of perovskite materials, cerium(III) bismuthate ($CeBiO_3$) and iron(III) bismuthate ($FeBiO_3$), for organic dye degradation under visible LED light illumination. The materials were synthesized via the sol-gel method and characterized using X-ray diffraction (XRD), Fourier-transform infrared spectroscopy (FT-IR), diffuse reflectance spectroscopy (DRS), and point of zero charge (PZC) analysis. A rhombohedral structure for $FeBiO_3$ and a tetragonal structure for $CeBiO_3$ with band gaps of 2.18 eV and 2.17 eV, respectively were revealed by structural characterization. The kinetic evolution of Methylene Blue (MB) degradation in an aqueous medium was examined. Both catalysts showed remarkable degradation efficiency, and $CeBiO_3$ demonstrated superior performance. Optimal degradation conditions were achieved at pH 10, with a catalyst concentration of 0.15 g/L, an initial Methylene Blue concentration of 10 mg/L, and a reaction time of 4 hours. Overall, this study highlights the potential of perovskite materials $CeBiO_3$ and $FeBiO_3$ to efficiently degrade organic dyes under visible light and contributes to the development of sustainable wastewater treatment solutions.

Keywords: perovskite, nanoparticles, sol-gel, cerium(III) bismuthate, iron(III) bismuthate, photocatalysis, dye degradation, band gap

Introduction

Nanomaterials are increasingly attracting attention across various fields, including environmental remediation, wastewater treatment, energy generation and storage, biomedicine. Their distinctive characteristics and processability into well-defined shapes and dimensions are essential for meeting specific application requirements [1–3]. In this context, perovskite-based materials, discovered in 1839 in the Ural Mountains by Gustave Rose and named after Count Lev Aleksevich von Perovski, have emerged as promising candidates. The earliest identified perovskite compound was $CaTiO_3$ [4].

Single perovskites are described by the general formula ABX_3, where A and B are cations, and X is an anion. Alkaline earth metals or lanthanides often occupy the A site, transition metals typically occupy the B site, and X can be oxygen or a halide. When the anion is oxygen, the structure is termed a perovskite oxide; when it is a halide, it is termed a perovskite halide. In single perovskite systems, the coordination number is 6 for the A site, 12 for the B site, and 6 for the O anions. An ideal BO_6 octahedral arrangement leads to a cubic lattice [4, 5].

Perovskite materials have been synthesized using various methods, including co-precipitation, sol-gel processes, microwave-assisted synthesis, hydrothermal and solvothermal methods, microemulsion techniques, and sonochemical routes [6–8]. Sol-gel technology has distinct advantages among these approaches, particularly in terms of its ability to produce solid-state materials from chemically homogeneous precursors. This method is simple and relatively eco-friendly, which makes it very attractive for the synthesis of nanoparticles [9]. Moreover, introducing randomness into the solution state improves the mixing of reactants at the atomic level, which is necessary for the synthesis of ternary and quaternary oxides at lower temperatures and over shorter time periods. The homogeneity and efficiency of the synthesis process is increased by this innovative approach, which in turn leads to a reduction in energy costs and contributes to progress in the production of materials for various industrial applications [10].

Photocatalysis uses a catalyst that absorbs light energy to speed up chemical reactions. The photocatalyst generates electron-hole pairs when irradiated with light, causing surface oxidation-reduction processes. These processes can degrade water pollutants or transform abundant earth elements, such as H_2O, CO_2,

and N_2 [11]. Semiconductor materials with relatively large band gaps, such as TiO_2 (3.2 eV) [12] and ZnO (3.37 eV) [13], are commonly utilized for photocatalytic dye decomposition. More recently, perovskite-type Bismuth Ferrite (BFO) has shown visible-light-driven catalytic activity, with a wide band gap ranging from 2.1 to 2.9 eV [14]. BFO nanoparticles are particularly appealing for dye degradation due to their high charge separation efficiency at room temperature and multiferroic properties. Moreover, materials with relatively lower band gap energies can efficiently support electron transfer to the conduction band under solar irradiation [4].

In the case of Methylene Blue (MB) dye, the initial deep-blue solution becomes colorless after degradation. Photodegradation is an oxidation process through which complex molecules are broken down into simple molecules. Following oxidation, MB decomposes into CO_2, H_2O, NH_4^+, and SO_4^{2-}. Electrons (e^-) are excited into the conduction band of the catalyst, forming an electron–hole (e^-, h^+) pair. Dissolved oxygen from the atmosphere subsequently captures electrons to generate superoxide radicals ($O_2\bullet^-$). Meanwhile, water molecules react with holes (h^+) in the valence band to form hydroxyl radicals (•OH). These $O_2\bullet^-$ and •OH radicals promote MB degradation according to the following equations [4]:

$$\text{Photocatalyst} + h\nu\ (\text{Visible Light}) \rightarrow e^-\ (\text{CB}) + h^+\ (\text{VB}) \quad (1)$$

$$O_2 + e^-\ (\text{CB}) \rightarrow O_2^{\bullet-} \quad (2)$$

$$H_2O + h^+\ (\text{VB}) \rightarrow \bullet OH + H^+ \quad (3)$$

$$MB + O_2^{\bullet-} \rightarrow \text{Degradation Products (including } CO_2, H_2O, NH_4^+, SO_4^{2-}) \quad (4)$$

$$MB + \bullet OH \rightarrow \text{Degradation Products (including } CO_2, H_2O, NH_4^+, SO_4^{2-}) \quad (5)$$

In this study, we investigated the synthesis and characterization of $CeBiO_3$ and $FeBiO_3$ nanoparticles via the sol-gel method and examined their photocatalytic activity for organic dye degradation under visible-light irradiation.

Experimental

Materials

Bismuth (III) nitrate ($Bi(NO_3)_3 \cdot 5H_2O$), iron nitrate ($Fe(NO_3)_3 \cdot 9H_2O$), and cerium (III) nitrate ($Ce(NO_3)_3 \cdot 4H_2O$) (Pro analysi MERCK), sodium hydroxide (NaOH), ethanol, citric acid and Methylene Blue were purchased from Sigma Aldrich. Distilled water was used as the solvent to prepare the oxides.

Synthesis Process

$CeBiO_3$ and $FeBiO_3$ nanoparticles were synthesized using the sol-gel method (Figure 1). For each compound, 0.1 mol aqueous solutions were prepared using $Bi(NO_3)_3 \cdot 5H_2O$, $Fe(NO_3)_3 \cdot 9H_2O$, and $Ce(NO_3)_3 \cdot 4H_2O$ dissolved in double-distilled water. A citric acid solution (1M) was introduced as a chelating agent. The pH was adjusted to 9 using NaOH (2M) under continuous magnetic stirring. The resulting solutions were thermally treated at 80 °C for 4h in a water bath under constant agitation. The obtained precipitates were filtered, washed thoroughly with distilled water and ethanol, and dried at 100 °C for 24 h. Finally, the powders were calcined at 800 °C for 4h in air atmosphere.

Characterization

The $CeBiO_3$ and $FeBiO_3$ nanoparticles were characterized using several techniques. X-ray diffraction (XRD) patterns were collected on a Rigaku MINIFLEX 600 diffractometer with monochromatic Cu Kα radiation (λ = 1.5418 Å) over 10–90° at a scanning rate of 5° min^{-1}. Fourier-transform infrared (FT-IR) spectra were recorded in the 500–4000 cm^{-1} range on a Bruker Alpha-P spectrophotometer. UV-visible diffuse reflectance spectra (DRS) were obtained to investigate the optical properties using a SHIMADZU UV-2600-PC spectrophotometer over 200–800 nm.

The point of zero charge (PZC) was determined using the pH drift method [15]. A series of 50 mL solutions of 0.01 M NaCl were added to closed vials and adjusted to initial pH values between 2 and 12 using (1M) hydrochloric acid (HCl) or sodium hydroxide (NaOH). Subsequently, 0.05 g of oxide was added to each solution and stirred for 48 h. The PZC was identified as the intersection point between the final pH versus initial pH curve and the line $pH_{final} = pH_{initial}$.

Figure 1. Sol-Gel Synthesis of $CeBiO_3$ and $FeBiO_3$ Nanoparticles

Photocatalytic activity Measurement

The photocatalytic activities of $CeBiO_3$ and $FeBiO_3$ were evaluated through MB degradation under visible-light irradiation using a CTRCH LED lamp (13 W). The catalyst (1.0 g/L) was dispersed in MB solution (20 mg/L, 100 mL) under continuous stirring. Prior to irradiation, the suspension was equilibrated in the dark for 30 min. During the degradation process, aliquots were collected at regular intervals and centrifuged (5000 rpm, 10 min) to remove the catalyst. The MB concentration was monitored by measuring the absorbance at 665 nm (the maximum absorption of MB) using a Shimadzu 1650 UV/Visible spectrophotometer.

Results and Discussion

Figure 2 presents the XRD pattern of the synthesized nanoparticles. Diffraction peaks appear at $2\theta = 22.5°$, 32.08°, 39.79°, 45.91°, 51.5°, and 57.35°, which correspond to the (012), (120), (110), (202), (024), and (300) crystal planes of face rhombohedral $FeBiO_3$ (JCPDS 01-073-0548) [16]. Likewise, Figure 3 exhibits the characteristic $CeBiO_3$ peaks in the 2θ range of 28.15°, 33.04°, 41.83°, and 55.9°, indexing to the (012), (200), (220), and (311) planes, respectively, and confirming a tetragonal structure in accordance with JCPDS 76-1730 [17].

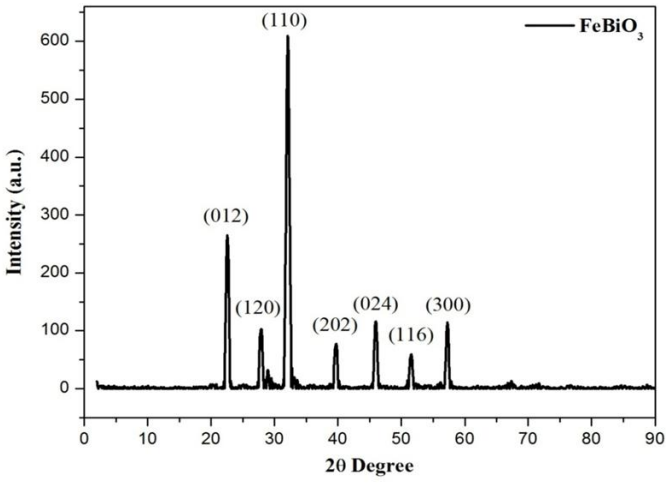

Figure 2. XRD Pattern of $FeBiO_3$

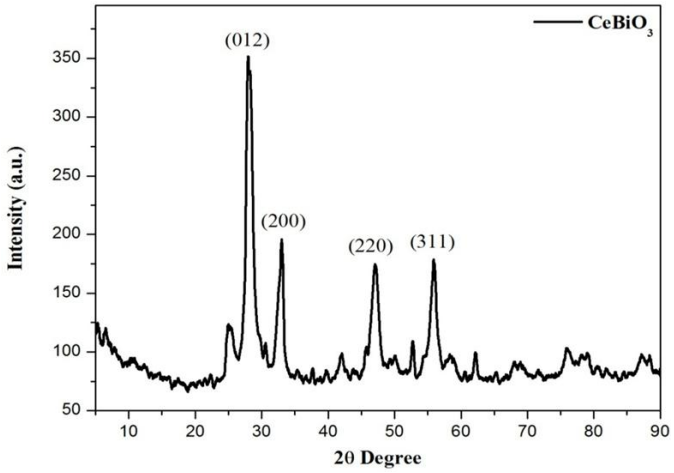

Figure 3. XRD Pattern of $CeBiO_3$

The particle sizes were calculated using the Debye-Scherrer equation [18]:

$$D = (0.9\lambda)/(\beta \cos \theta) \quad (6)$$

Where D is the particle size (nm), λ is the X-ray wavelength (as used in the experiment), θ is the diffraction angle, and β is the full width at half maximum (FWHM), expressed in radians. The calculated sizes are listed in Table 1.

Table 1

Crystallite Size Analysis of the Synthesized Perovskites

Sample	2θ (°)	(hkℓ)	D (nm)
$FeBiO_3$	32.08	(110)	36.06
$CeBiO_3$	28.01	(012)	35.82

The calculated particle sizes for the $CeBiO_3$ and $FeBiO_3$ samples calcined at 800 °C were 35.82 nm and 36.06 nm, respectively, which are relatively large and indicate the successful formation of nanoparticles.

The FT-IR spectrum of the synthesized nanoparticles (Figure 4) indicates the presence of adsorption bands at 915 and 809 cm^{-1}, which are attributed to the valence vibration modes of the Bi–O bond in $CeBiO_3$ and $FeBiO_3$, respectively [19]. Additionally, the bands at 570 cm^{-1} and 670 cm^{-1} correspond to the valence vibration modes of the Ce–O and Fe–O bonds in $CeBiO_3$ and $FeBiO_3$, respectively [20, 21].

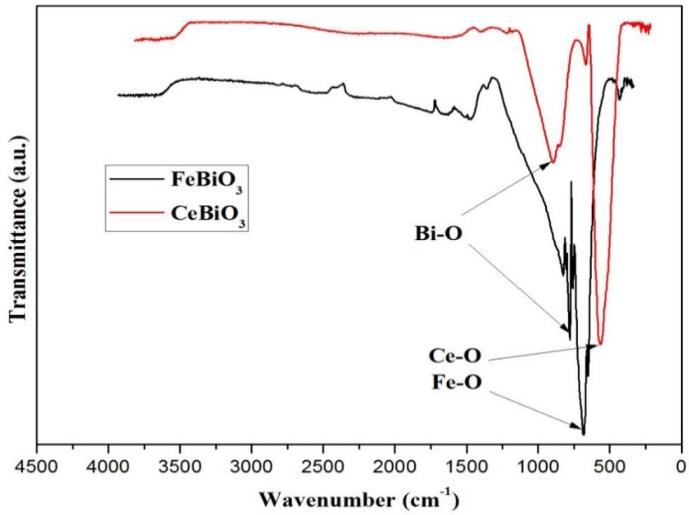

Figure 4. Fourier-transform infrared spectroscopy (FT-IR) of $CeBiO_3$ and $FeBiO_3$

The band gap energies of $CeBiO_3$ and $FeBiO_3$ were determined from their diffuse-reflection spectra using the Kubelka–Munk function [22], defined as:

$$F(R) = (1 - R) / (2R) \quad (7)$$

Where R is the observed reflection in the UV/Vis spectrum. The optical band gap was obtained by identifying the intersection point on the $(F(R)\ h\nu)^2$ — $h\nu$ plot (Figures 5 and 6), where h represents Planck's constant and ν is the photon frequency. By applying this method, the resulting band gaps were 2.18 eV for $FeBiO_3$ and 2.17 eV for $CeBiO_3$ [23].

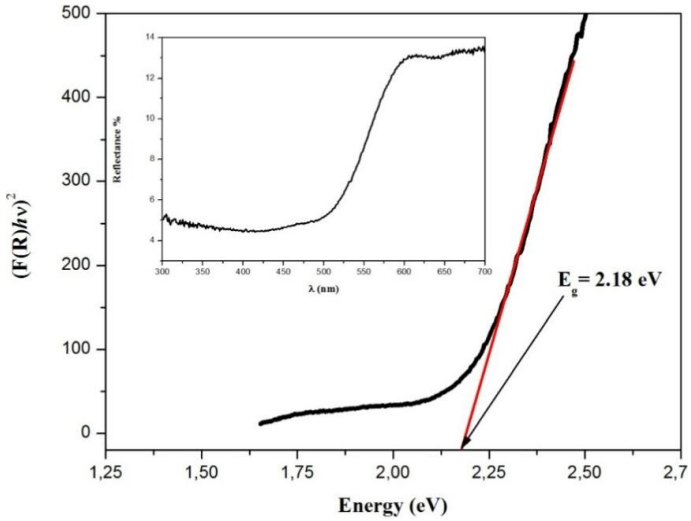

Figure 5. Optical Band Gap Determination of $FeBiO_3$

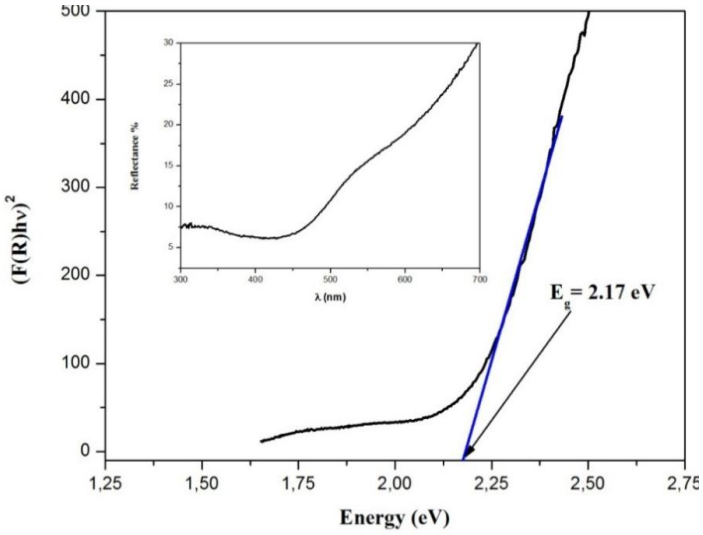

Figure 6. Optical Band Gap Determination of $CeBiO_3$

The point of zero charge was determined for both materials by plotting the final and initial pH (Figures 7 and 8). The pH_{pzc} values, identified at the intersection of the measurement curve with the bisector line from the data without adding $CeBiO_3$ and $FeBiO_3$, were 6.2 and 5.6 for $CeBiO_3$ and $FeBiO_3$, respectively. These values define the pH-dependent surface charge characteristics of the nanoparticles: the surface becomes negatively charged above pH_{pzc} and positively charged below pH_{pzc} (Figures 9 and 10) [24].

The photocatalytic degradation of MB was monitored under visible-light irradiation (Figure 11). Prior to irradiation, the suspensions were equilibrated in the dark, showing a minimal decrease in the MB concentration due to adsorption. Under visible light, $CeBiO_3$ demonstrated superior photocatalytic activity, achieving 85 % MB degradation after 4 h, whereas $FeBiO_3$ reached 48.5 % degradation under identical conditions.

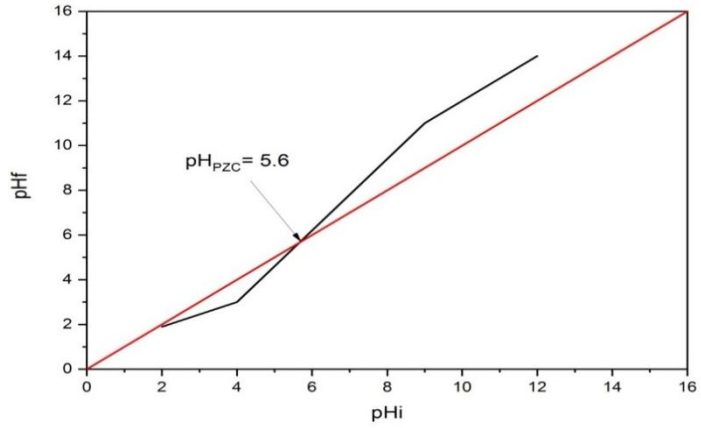

Figure 7. Determination of the pH_{pzc} for $FeBiO_3$

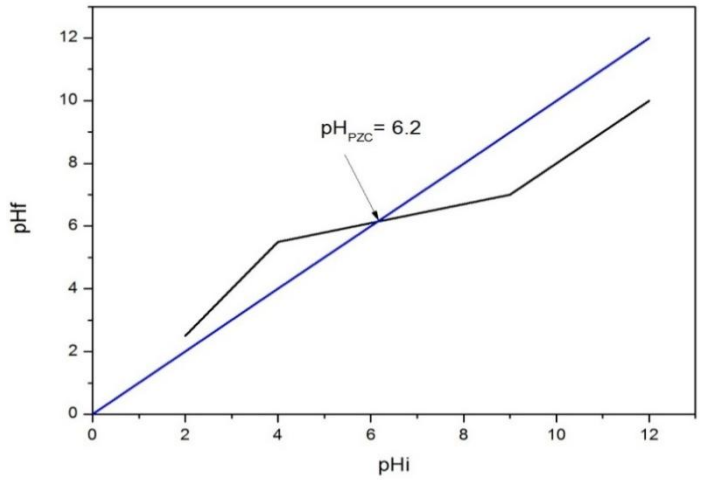

Figure 8. Determination of the pH_{pzc} for $CeBiO_3$

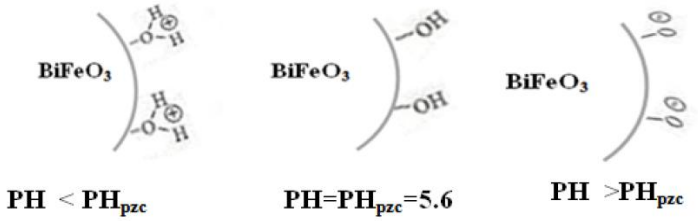

Figure 9. Variation in the Surface Charge of $FeBiO_3$ as a Function of pH

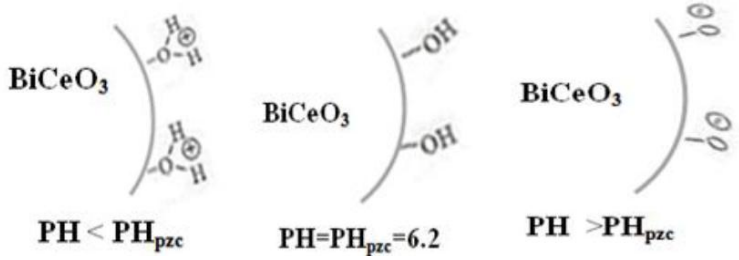

Figure 10. Variation in the Surface Charge of $CeBiO_3$ as a Function of pH

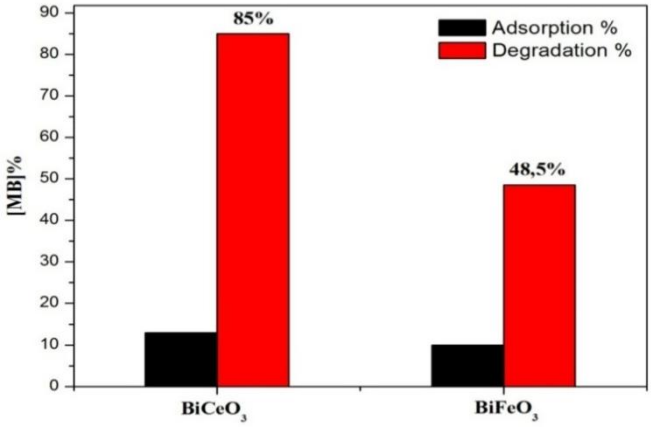

Figure 11. Adsorption and Photocatalytic Degradation of MB
([Catalyst] = 0.1 g; [MB] = 10 mg·L^{-1}; [V] = 100 mL; [T] = 4 h)

The effects of operational parameters, including pH, photocatalyst dosage, and initial MB concentration, on the photocatalytic performance were investigated. The effect of pH was assessed by adjusting the solution pH to 3, 6, and 10 using (1M) HCl and NaOH while maintaining a constant MB concentration (10 mg L^{-1}) and catalyst loading (0.1 g). The results demonstrated that alkaline conditions enhanced the photodegradation efficiency, achieving 91 % removal for both $CeBiO_3$ and $FeBiO_3$ catalysts. In contrast, acidic media exhibited substantially lower degradation rates of 46 % and 65 % for $CeBiO_3$ and $FeBiO_3$, respectively (Figure 12). These findings are consistent with the previously reported pH-dependent photocatalytic behavior [25, 26].

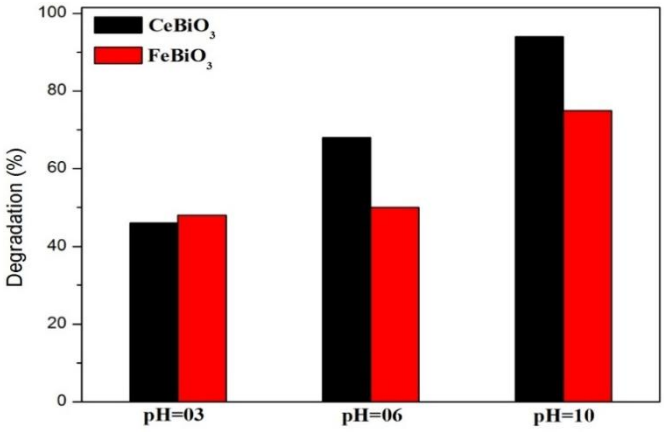

Figure 12. Effect of pH on the Photocatalytic Degradation of MB
([Catalyst] = 1.0 g·L^{-1}); [MB] = 10 mg·L^{-1}))

The impact of pH on MB degradation was investigated under varying pH conditions. The degradation efficiency exhibited minimal activity under acidic conditions (pH = 3) and near-neutral pH (pH = 6). However, alkaline conditions (pH = 10) demonstrated an enhanced photocatalytic performance, with a degradation efficiency of 91 %. This enhancement can be attributed to the increased concentration of hydroxide ions (OH^-) in the basic medium, which promotes the formation of hydroxyl radicals (•OH) through hole (h^+) oxidation, as described by the following equation:

$$OH^- + h^+ \rightarrow \bullet OH \quad (8)$$

This result aligns with previous studies that reported enhanced photocatalytic activity under basic conditions owing to favorable radical formation kinetics [25, 26].

The influence of the photocatalyst dosage on the MB photodegradation efficiency was investigated. Photocatalytic tests were conducted using varying quantities of the catalyst in an aqueous MB solution with an initial 10 mg L^{-1} concentration under ambient pH conditions. As shown in Figure 13, the photocatalytic degradation performance exhibited an inverse relationship with increasing catalyst concentration. This phe-

nomenon can be attributed to the screening effect manifested at higher catalyst loadings, whereby excessive catalyst particles induce enhanced solution turbidity, consequently diminishing visible light penetration through the reaction medium [25–27]. The optimal photocatalytic performance was achieved within a catalyst dosage range of 0.1–0.15 mg, beyond which a significant reduction in the degradation efficiency was observed.

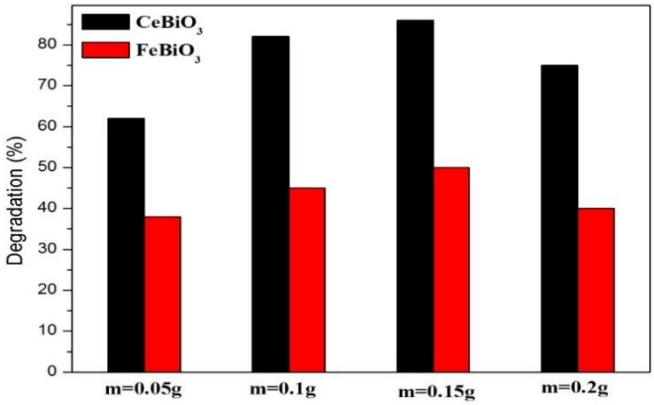

Figure 13. Effect of Catalyst Dosage on the Degradation of MB (10 mg·L^{-1})

The photocatalytic degradation performance was evaluated as a function of the initial MB concentration, ranging from 5 to 20 mg L^{-1}, utilizing 0.1 g of photocatalyst in 100 mL reaction volume. Figure 14 illustrates the photodegradation efficiencies of CeBiO3 and FeBiO3 under varying MB concentrations. The degradation rate was inversely correlated with the MB concentration. This behavior is attributed to the screening effect at elevated MB concentrations, wherein the solution opacity increases, thereby reducing the visible light penetration through the reaction medium. Both synthesized oxide photocatalysts demonstrated comparable concentration-dependent behavior under the investigated conditions [28].

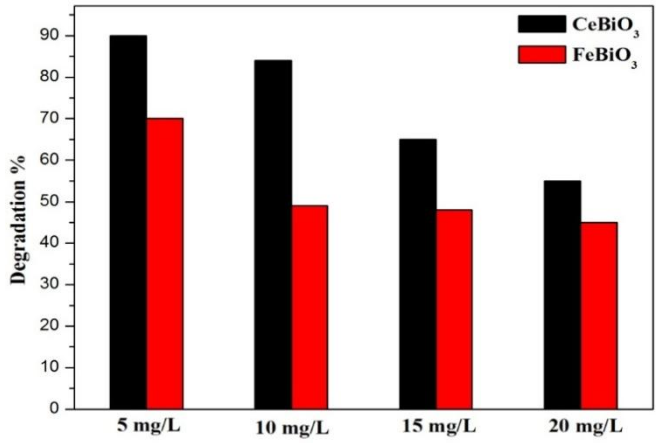

Figure 14. Effect of Initial MB Concentration on Photocatalytic Degradation Efficiency

Conclusions

$CeBiO_3$ and $FeBiO_3$ perovskite-structured photocatalysts were synthesized through the sol-gel method followed by calcination at 800 °C and evaluated for MB degradation under visible LED illumination. XRD analysis confirmed the rhombohedral $FeBiO_3$ and tetragonal $CeBiO_3$ structures, while FT-IR spectroscopy showed characteristic metal-oxygen bonds at 541/571 cm^{-1} for the calcined powders and 626/622 cm^{-1} for Ce–O and Fe–O vibrations. Both materials exhibited comparable band gaps (2.18 eV for $FeBiO_3$ and 2.17 eV for $CeBiO_3$) and distinct surface charge characteristics (pH_{pzc} = 5.6 and 6.2, respectively).

$CeBiO_3$ exhibited enhanced photocatalytic efficiency compared to $FeBiO_3$, achieving a 91 % degradation efficiency under optimized conditions, including pH 10, a catalyst loading of 0.10–0.15 g/L, and an initial MB concentration of 10 mg/L, within 4 hours of irradiation. An inverse correlation was shown for the

initial degradation rate and MB concentration, which reduced the overall efficiency at higher concentrations due to optical screening effects. The photocatalytic efficiency and visible light absorption properties of these materials, especially $CeBiO_3$, make them potentially suitable for practical water treatment applications. A sustainable approach for water decontamination is provided by the environmentally benign nature of these materials, combined with visible-light activation.

*Author Information**

**The authors' names are presented in the following order: First Name, Middle Name and Last Name*

Mohamed Badaoui — Doctor and Researcher, Synthesis and Catalysis Laboratory, University of Tiaret, BP P 78, Zaaroura, Tiaret, Algeria; e-mail: mohamed.badaoui@univ-tiaret.dz; https://orcid.org/0000-0001-7455-7184

Hafida Sehil — Doctor and Researcher, Department of Chemistry, Faculty of Sciences of the Matter, University of Tiaret, BP P 78, Zaaroura, Tiaret, Algeria; e-mail: hafida.sehil@univ-tiaret.dz

Chaimaa Lamouri — Master Student, Department of Chemistry, Faculty of Sciences of the Matter, University of Tiaret, BP P 78, Zaaroura, Tiaret, Algeria; e-mail: lamourichaima.38@gmail.com

Author Contributions

The manuscript was written through contributions of all authors. All authors have given approval to the final version of the manuscript. CRediT: **Mohamed Badaoui** was responsible for conceptualization, data curation, investigation, methodology, validation, visualization, and writing review and editing. **Hafida Sehil** contributed through data curation, formal analysis, visualization, supervision, drafting the original manuscript and reviewing its content. **Chaimaa Lamouri** was involved in data curation, formal analysis, and resource provision.

Conflicts of Interest

The authors declare no conflicts of interest.

References

1 Osman, A.I., et al. (2024). Synthesis of green nanoparticles for energy, biomedical, environmental, agricultural, and food applications: A review. *Environ. Chem. Lett., 22*, 841–887. https://doi.org/10.1007/s10311-023-01682-3

2 Rathod, S., Preetam, S., Pandey, C., & Bera, S.P. (2024). Exploring synthesis and applications of green nanoparticles and the role of nanotechnology in wastewater treatment. *Biotechnol. Rep., 41*, e00830. https://doi.org/10.1016/j.btre.2024.e00830

3 Attfield, J.P., Lightfoot, P., & Morris, R.E. (2015). Perovskites. *Dalton Trans., 44*, 10541–10542. https://doi.org/10.1039/C5DT90083B

4 Irshad, M., et al. (2022). Photocatalysis and perovskite oxide-based materials: A remedy for a clean and sustainable future. *RSC Adv., 12*, 7009–7039. https://doi.org/10.1039/D1RA08185C

5 Zhou, D., Zhou, T., Tian, Y., Zhu, X., & Tu, Y. (2018). Perovskite-based solar cells: Materials, methods, and future perspectives. *J. Nanomater., 2018*, Art. ID 8148072, 1–15. https://doi.org/10.1155/2018/8148072

6 Ke, H., Wang, W., Wang, Y., Xu, J., Jia, D., Lu, Z., & Zhou, Y. (2011). Factors controlling pure-phase multiferroic $BiFeO_3$ powders synthesized by chemical co-precipitation. *Journal of Alloys and Compounds, 509*(5), 2192–2197. https://doi.org/10.1016/j.jallcom.2010.09.213

7 Comyn, T.P., Kanguwe, D.F., He, J., & Brown, A.P. (2008). Synthesis of bismuth ferrite lead titanate nano-powders and ceramics using chemical co-precipitation. *Journal of the European Ceramic Society, 28*(11), 2233–2238. https://doi.org/10.1016/j.jeurceramsoc.2008.02.013

8 Kim, J.K., Kim, S.S., & Kim, W.-J. (2005). Sol–gel synthesis and properties of multiferroic $BiFeO_3$. *Materials Letters, 59*(29–30), 4006–4009. https://doi.org/10.1016/j.matlet.2005.07.050

9 Kakihana, M. (1996). Invited review 'sol-gel' preparation of high temperature superconducting oxides. *Journal of Sol-Gel Science and Technology, 6*(1), 7–55. https://doi.org/10.1007/bf00402588

10 Danks, A.E., Hall, S.R., & Schnepp, Z. (2016). The evolution of 'sol–gel' chemistry as a technique for materials synthesis. *Mater. Horiz., 3*, 91–112. https://doi.org/10.1039/C5MH00185G

11 Hassaan, M.A., El-Nemr, M.A., Elkatory, M.R., Ragab, S., Niculescu, V.C., & El-Nemr, A. (2023). Principles of photocatalysts and their different applications: A review. *Top Curr. Chem., (Z) 381*, 31. https://doi.org/10.1007/s41061-023-00444-7

12 Tasisa, Y.E., Sarma, T.K., Krishnaraj, R., & Sarma, S. (2024). Band gap engineering of titanium dioxide (TiO_2) nanoparticles prepared via green route and its visible-light-driven environmental remediation. *Results Chem., 11*, 101850. https://doi.org/10.1016/j.rechem.2024.101850

13 Jafarova, V.N., & Orudzhev, G.S. (2021). Structural and electronic properties of ZnO: A first-principles DFT study within LDA(GGA) and LDA(GGA)+U methods. *Solid State Commun., 325*, 114166. https://doi.org/10.1016/j.ssc.2020.114166

14 Mandal, G., Goswami, M.N., & Mahapatra, P.K. (2024). Efficient photocatalytic degradation of wastewater solution through Mn-doped $BiFeO_3$ nanomaterials. *Physica B Condens. Matter, 695*, 416475. https://doi.org/10.1016/j.physb.2024.416475

15 López-Ramón, M.V., Stöeckli, F., Moreno-Castilla, C., & Carrasco-Marín, F. (1999). On the characterization of acidic and basic surface sites on carbons by various techniques. *Carbon, 37*, 1215–1221. https://doi.org/10.1016/S0008-6223(98)00317-0

16 Mohd Azmy, H.A., et al. (2017). Visible-light photocatalytic activity of $BiFeO_3$ nanoparticles for degradation of methylene blue. *J. Phys. Sci., 28*, 85–103. https://doi.org/10.21315/jps2017.28.2.6

17 Das, B.B., & Rao, R.G. (2015). Synthesis, crystal structure, and electronic properties of $CeBiO_3$ oxide. *Phys. Status Solidi B, 252*, 2680–2684. https://doi.org/10.1002/pssb.201451753

18 West, A.R. (2014). Solid State Chemistry and Its Applications, 2nd ed.; Wiley: Chichester, West Sussex, UK.

19 Meena, P.L., Surela, A.K., Saini, J.K., & Chhachhia, L.K. (2022). Millettia pinnata plant pod extract-mediated synthesis of Bi_2O_3 for degradation of water pollutants. *Environ. Sci. Pollut. Res., 29*, 79253–79271. https://doi.org/10.1007/s11356-022-21435-z

20 Wattanathana, W., et al. (2021). Crystallographic and spectroscopic investigations on oxidative coordination in the heteroleptic mononuclear complex of cerium and benzoxazine dimer. *Molecules, 26*, 5410. https://doi.org/10.3390/molecules26175410

21 Hu, Y., Fei, L., Zhang, Y., Yuan, J., Wang, Y., & Gu, H. (2011). Synthesis of bismuth ferrite nanoparticles via a wet chemical route at low temperature. *J. Nanomater., 2011*, Art. ID 797639, 1–6. https://doi.org/10.1155/2011/797639

22 Martins, A.C., et al. (2017). Sol–gel synthesis of new TiO_2/activated carbon photocatalyst and its application for degradation of tetracycline. *Ceram. Int. 43*, 4411–4418. https://doi.org/10.1016/j.ceramint.2016.12.088

23 Sonia, A., Kumar, A., & Kumar, P. (2023). Z-scheme $ZnFe_2O_4/CeO_2$ nanocomposites with enhanced photocatalytic performance under UV light. *Appl. Phys. A, 129*, 724. https://doi.org/10.1007/s00339-023-06959-6

24 Subramani, A.K., Byrappa, K., Ananda, S., Lokanatha Rai, K.M., Ranganathaiah, C., & Yoshimura, M. (2007). Photocatalytic degradation of indigo carmine dye using TiO_2-impregnated activated carbon. *Bull. Mater. Sci., 30*, 37–41. https://doi.org/10.1007/s12034-007-0007-8

25 Gupta, V.K., Jain, R., Agarwal, S., Nayak, A., & Shrivastava, M. (2012). Photodegradation of hazardous dye quinoline yellow catalyzed by TiO_2. *J. Colloid Interface Sci., 366*, 135–140. https://doi.org/10.1016/j.jcis.2011.08.059

26 Tsaviv, J.N., Eneji, S.I., Sha'Ato, R., Ahemen, I., Jubu, P.R., & Yusof, Y. (2024). Photodegradation, kinetics, and non-linear error functions of methylene blue dye using $SrZrO_2$ perovskite photocatalyst. *Heliyon, 10*, e34517. https://doi.org/10.1016/j.heliyon.2024.e34517

27 Yazdanbakhsh, M., Tavakkoli, H., & Hosseini, S.M. (2011). Characterization and evaluation of catalytic efficiency of $La_{0.5}Ca_{0.5}NiO_2$ nanopowders in removal of reactive blue 5 from aqueous solution. *Desalination, 281*, 388–395. https://doi.org/10.1016/j.desal.2011.08.020

28 Fosso-Kankeu, E., Pandey, S., & Ray, S.S. (Eds.). (2020). Photocatalysts in Advanced Oxidation Processes for Wastewater Treatment; Scrivener Publishing: Hoboken, NJ. https://doi.org/10.1002/9781119631422